Environmentally dependent dust chemistry of a super Asian dust storm in March 2010: observation and simulation

Qiongzhen Wang[1, 2], Xinyi Dong[3], Joshua S. Fu[3], Jian Xu[1], Congrui Deng[1], Yilun Jiang[1], Qingyan Fu[4], Yanfen Lin[4], Kan Huang[1,5]*, Guoshun Zhuang[1]*

[1]Center for Atmospheric Chemistry Study, Shanghai Key Laboratory of Atmospheric Particle Pollution and Prevention (LAP3), Department of Environmental Science and Engineering, Fudan University, Shanghai, 200433, P. R. China

[2]Environmental Science Research & Design Institute of Zhejiang Province, Hangzhou, 310007, P. R. China

[3]Department of Civil and Environmental Engineering, University of Tennessee, Knoxville, TN, 37996, USA

[4]Shanghai Environmental Monitoring Center, Shanghai, 200030, China

[5]Institute of Atmospheric Sciences, Fudan University, Shanghai, 200433, P. R. China

Correspondence: huangkan@fudan.edu.cn; gzhuang@fudan.edu.cn

Abstract

Near surface and vertical *in situ* measurements of atmospheric particles were conducted in Shanghai during March 19-23, 2010 to explore the transport and chemical evolution of dust particles in a super dust storm. An air quality model with optimized physical dust emission scheme and newly implemented dust chemistry was utilized to study the impact of dust chemistry on regional air quality. Two discontinuous dust periods were observed with one travelling over Northern China (DS1) and the other passing over the coastal regions of Eastern China (DS2). Stronger mixing extents between dust and anthropogenic emissions were found in DS2, reflecting by the higher SO_2/PM_{10} and NO_2/PM_{10} ratios as well as typical pollution elemental species such as As, Cd, Pb, and Zn. As a result, the concentrations of SO_4^{2-}

and NO_3^- and the ratio of Ca^{2+}/Ca were more elevated in DS2 than in DS1 but opposite for the $[NH_4^+]/[SO_4^{2-}+NO_3^-]$ ratio, suggesting the heterogeneous reactions between calcites and acid gases were significantly promoted in DS2 due to the higher level of relative humidity and gaseous pollution precursors. Lidar observation showed a columnar effect on the vertical structure of particle optical properties in DS1 that dust dominantly accounted for ~80-90% of the total particle extinction from near the ground to ~700m. In contrast, the dust plumes in DS2 were refrained within lower altitudes while the extinction from spherical particles exhibited maximum at a high altitude of ~800m. The model simulation reproduced relatively consistent results with observations that strong impacts of dust heterogeneous reactions on secondary aerosol formation occurred in areas where the anthropogenic emissions were intensive. Compared to the sulfate simulation, the nitrate formation on dust is suggested to be improved in the future modeling efforts.

1. Introduction

Asian dust originating from the arid and semiarid areas in Mongolia and China can be transported for long distances, reaching Beijing (Sun et al., 2010), Shanghai (Fu et al., 2010), Xiamen (Zhao et al., 2011), Taiwan (Tsai et al., 2012; Tsai et al., 2014), and even as far as North America (Uno et al., 2009; Wu et al., 2015), exerting significant impacts on the air quality of both densely populated habitations and remote regions. Huang et al. (2014) showed that Asian dust could transport from the Qilian Mountain or from the Qaidam Basin through Qinghai and Gansu provinces to reach the Pacific Ocean, and that dust originating from the Taklimakan Desert could travel across the Hexi Corridor and Loess Plateau to reach southeastern China. Zhao et al. (2009) demonstrated that the deserts in Mongolia and in western and northern China were the major sources of Asian dust particles in East Asia and estimated that 26% of the dust particles emitted from Asian dust sources was transported to the Pacific Ocean. Eguchi et al. (2009) reported that the dust plume from the Gobi Desert in East Asia

was transported at low altitudes of 4-6km to North America and mixed with Asian anthropogenic air pollutants during its transport. Fu et al. (2014) simulated that during a dust event from May 1 to 6, 2011, the transported dust particles accounted for 78.9% of the surface layer PM_{10} over the Yangtze River Delta.

Dust particles can significantly influence the regional/global climate directly by absorbing and scattering solar radiation (Bi et al., 2016) and also indirectly by influencing the formation of ice nuclei, cloud, and precipitation (Creamean et al., 2013; Li and Min, 2010; Wang et al., 2010). In addition, deposition of transported dust particles into the ocean can enhance phytoplankton blooms due to the existence of bioavailable iron (Wang et al., 2012; Zhuang et al., 1992), which indirectly impacts on global climate change. The effects of dust particles on climate change depend critically on their physical and chemical properties. Natural dust particles with limited contamination have low light-absorption, with single-scattering albedo of 0.91-0.97 at 500nm and 550nm (Bi et al., 2014; Uchiyama et al., 2005). During the long-range transport, dust particles are often modified by their mixing with anthropogenic emissions over the downwind areas (Fischer et al., 2011; Formenti et al., 2011; Huang et al., 2010b; Tobo et al., 2010), resulting in high uncertainties in evaluating the climatic effects of dust particles. It was estimated that mineral dust had a radiative forcing of -0.1 ± 0.2 Wm^{-2} (IPCC, 2013), of which the uncertainty was as high as 200%. Obviously, the characteristics of dust particles and their evolution during the transport are not well understood.

In March 2010, a super dust storm swept China, invading extensive areas from Northern China to Southern China including Fujian and Guangdong provinces, and lasting for ~4 days from March 19 to 23 (Li et al., 2011). The dust plumes further extended to the South China Sea (Wang et al., 2011), Taiwan (Tsai et al., 2013), Korea (Tatarov et al., 2012), Japan (Zaizen et al., 2014), and even to North America (Wu et al., 2015). This dust storm was as strong as the one in March 20-21, 2002 and attracted considerable attentions. Chen et al. (2017) used WRF-Chem to simulate the

emission and transport of dust particles over the Taklimakan Desert and Gobi Desert. The results indicated that the Gobi Desert dust particles were easily lifted to 4km and subject to the long-range transport, which contributed much more to the dust plumes over East Asia than the Taklimakan Desert dust. Lidar observations revealed that this super dust storm was transported within a low altitude (Tatarov et al., 2012; Wang et al., 2011), which could benefit the mixing and interaction between dust particles and anthropogenic pollutants. Indeed, modifications of dust particles during the transport of this dust storm were suggested based on in situ measurements. Zhao et al. (2011) displayed substantial increases of particulate sulfate and nitrate when the dust plumes arrived at Xiamen city of Fujian province, implying the mixing and interaction between dust particles and anthropogenic pollutants. Wang et al. (2011) indicated that the dust particles detected at the Dongsha Island over the South China Sea were mixed with anthropogenic and marine particles. Observations of this dust storm at Tsukuba and Mt. Haruna, Japan showed that most of the transported dust particles in lower altitudes were internally mixed with sulfate or seasalt (Zaizen et al., 2014).

Most of the studies on this super dust storm focused on investigating the dust particles reaching Southeastern China and the South China Sea, and relied on single method, e.g. aerosol chemistry measurement, optical property inversion, or model simulation. In this study, we investigated this super dust storm in Shanghai, a coastal city in Eastern China. A synergy of measurement techniques was applied, including in situ measurements of pollutant gaseous precursors, particle with its major chemical components, and Lidar observation of particle optical properties. To corroborate the observational evidence, a regional numerical model was used to simulate the impact of dust chemistry on the perturbation of regional air quality. What interested us is that there were two discontinuous dust periods observed in Shanghai with distinctly different transport pathways, providing a great opportunity to study the chemical evolution of transported dust particles under different environmental conditions.

2. Methodology

2.1. Field measurement

2.1.1. Lidar observation

A dual-wavelength depolarization Lidar (Model:L2S-SMII) developed by the National Institute for Environmental Studies (NIES) of Japan was installed on the roof (~20m above ground level) of a teaching building on the campus of Fudan University in the Yangpu District of Shanghai (Fig. 1b). The Lidar measurement was performed every 15 min (at 00, 15, 30, and 45 minutes every hour) with a height resolution of 6 m. Attenuated backscattering coefficient (β), volume depolarization ratio (δv), particle depolarization ratio (δp), and particle extinction coefficient (σ) at the wavelength of 532 nm were obtained by the measurement. More details about the Lidar system have been described in Huang et al. (2012). δv is calculated using the parallel (Ip) and perpendicular (Is) components of backscatter intensity, and Ip and Is were calibrated before the calculation. Briefly, a sheet polarizer with the polarizing direction set at 45 degree (then -45 degree) to the polarizing plane of the emitted light was installed in front of the beam splitter cube, and two sets of backscatter signal profiles from the sky were obtained for the calibration. Detailed calibration procedure has been described in Shimizu et al. (2004) and Shimizu et al. (2017). σ was derived by the Fernald inversion method (Fernald, 1984) with the lidar ratio (extinction-to-backscatter ratio) set as 50 sr (Liu et al., 2002) in the inversion process. The total particle extinction coefficient can be split to non-spherical particle (dust particle, σ_d) and spherical particle (mostly pollution particle, σ_s) fractions based on the value of δp. The splitting method was described in detail by Sugimoto et al. (2002) and Shimizu et al. (2004).

To solve the problem that overlap of the laser beam and the view field of telescope is insufficient for near surface observation, a compensation function Y(z) was applied. Function Y(z) was derived from the signal profiles that observed on a day when the planetary boundary layer was well developed. With the compensation, the optical properties of the particles above 120 m altitude were provided. Detailed correction

141 procedure has been described in Shimizu et al. (2017).

142

143 **2.1.2. Online particle and gases monitoring**

144 Continuous PM_{10} concentrations were measured by a TEOM (Tapered Element
145 Oscillating Microbalance) 1405D monitor (Thermo Scientific, USA). Trace gases SO_2
146 and NO_2 were measured by a 43i SO_2 analyzer (Thermo Scientific, USA) and a 42i
147 NO-NO_2-NOx analyzer (Thermo Scientific, USA), respectively. All the measured
148 PM_{10} and gases concentrations were averaged and used at intervals of 1hr in this
149 study.

150

151 **2.1.3. Aerosol sampling**

152 TSP (Total Suspended Particles) samples were collected during March 19-27, 2010
153 at the Fudan observational site co-located with all the other instruments. The aerosol
154 samples were collected for 12 hours (normally from 8:00 to 20:00LST (Local
155 Standard Time) in daytime and from 20:00 to 8:00 LST of the next day in nighttime)
156 or 24 hours (normally from 8:00 to 8:00 LST of the next day) on Whatman 41 filters
157 (Whatman Inc., Maidstone, UK) by a medium-volume sampler (Beijing Geological
158 Instrument-Dickel Co., Ltd.; model: TSP/PM_{10}/$PM_{2.5}$-2; flow rate: 77.59 L min^{-1}). All
159 the samples were put in polyethylene plastic bags immediately after sampling and
160 then reserved in a refrigerator. The filters were weighed before and after sampling
161 using an analytical balance (Model: Sartorius 2004MP; reading precision: 10μg) after
162 stabilizing in constant temperature (20±1°C) and humidity (40±2%) for 48 hours. All
163 the procedures were strictly quality controlled to avoid the possible contamination of
164 the samples.

165

166 **2.2. Chemical analysis**

167 **2.2.1. Ion analysis**

168 One fourth of each aerosol sample and blank filters were extracted ultrasonically by

10 ml deionized water (18 MΩ cm^{-1}). Inorganic ions of SO_4^{2-}, NO_3^-, Cl^-, Na^+, NH_4^+, K^+, Mg^{2+}, and Ca^{2+} were analyzed by an Ion Chromatography (Dionex ICS 3000, USA) with a separation column of DionexIonpac AS 11, a guard column of Dionex Ionpac AG 11, a self-regenerating suppressed conductivity detector of Dionex Ionpac ED50, and a gradient pump of Dionex Ionpac GP50. The detailed analytical procedures can be found in Yuan et al. (2003).

2.2.2. Element analysis

Half of each aerosol sample and blank filters were digested at 170 °C for 4 hours in a high pressure Teflon digestion vessel with 3ml concentrated HNO_3, 1ml concentrated $HClO_4$, and 1 ml concentrated HF. The solutions were dried, and then diluted to 10 ml with deionized water (18 MΩ cm^{-1}). Fifteen elements (Al, As, Ca, Cd, Cu, Fe, Mg, Mn, Na, Ni, Pb, Sr, Ti, V, and Zn) were measured by an inductively coupled plasma optical emission spectroscopy (ICP-OES; SPECTRO, Germany). The detailed analytical procedures were described in Sun et al. (2004a) and Zhuang et al. (2001).

2.3. Nation-wide daily PM_{10} data

Air pollution index (API) data in 86 major cities (locations shown in Fig. 1a) over China were obtained from the data center of Ministry of Environmental Protection of China (http://datacenter.mep.gov.cn/). In China, six grades of air pollution of excellent, good, slightly polluted, lightly polluted, moderately polluted, and heavily polluted were set corresponding to the API scales of 0-50, 51-100, 101-150, 151-200, 201-300, and >300, respectively. Both API values of 50, 100, 200, 300, 400, and 500 and their corresponding concentrations of air pollutants were defined in the API grading limited value table as shown in Table S1. According to the definition of API in China, the API value of air pollutants was calculated as

$$I_x = (I_{x,\,high} - I_{x,\,low})(C_x - C_{x,\,low})/(C_{x,\,high} - C_{x,\,low}) + I_{x,\,low},$$

where C_x and I_x are the concentration and the API value of air pollutant X in Table S1, respectively. $I_{x, high}$ and $I_{x, low}$ stand for the two values in the API grading limited value table (Table S1) that mostly approach to value I_x, respectively. $C_{x, high}$ and $C_{x, low}$ represent the concentration of X corresponding to $I_{x, high}$ and $I_{x, low}$, respectively. And the daily API value is defined as

$$API = Max(I_{PM10}, I_{SO2}, I_{NO2}, I_{CO}, I_{O3}).$$

According to API data records from March 20 to 23, 2010, PM_{10} was the premier air pollutant in most of the 86 cities over China, i.e. $API= I_{PM10}$. Thus, the API value can be converted to PM_{10} concentration as

$$C = (I - I_{low})(C_{high} - C_{low})/(I_{high} - I_{low}) + C_{low}.$$

It should be noted that API was recorded with a maximum value of 500, which corresponded to the PM_{10} concentration of 600 μgm^{-3}.

2.4. Backward trajectory analysis

48 hours back trajectories of the air masses at both 250 m and 1000 m AGL (Above Ground Level) during dust days starting at Shanghai were computed by the HYSPLIT model (http://ready.arl.noaa.gov/hypub-bin/trajtype.pl?runtype=archive), using the meteorological data of GDAS (1 degree, global, 2006-present). Four trajectories ending at 0, 6, 12, and 18 LST were calculated for each day.

2.5. Model simulation

The WRF/CMAQ modeling system was applied to simulate the dust chemistry in this study. The Weather Research and Forecasting model (WRFv3.4) was used to produce the meteorology fields by digesting the reanalysis data from National Centers for Environmental Prediction (NCEP). The Community Multiscale Air Quality Modeling System (CMAQv5.0.1) was configured with the 2005 carbon bond gas-phase mechanism (CB05) and aerosol module AE6. The default CMAQ model doesn't include dust chemistry reactions but only the dust emission module. We have

implemented dust chemistry in the CMAQ model and corrected the dust emission module in our earlier work (Dong et al., 2015), which was used to simulate the heterogeneous reactions on dust during the long-range transport in this study. Briefly, the major developments included: (1) The default dust emission module in CMAQ was found to strongly underestimate the dust emissions. By removing the double counting of soil moisture in the default dust emission module and conducting a reanalysis of field data, the threshold friction velocities over various land covers were re-adjusted. (2) The source-dependent speciation profiles of dust particles from the Taklimakan and Gobi Desert were implemented based on field measurement data. (3) Thirteen dust heterogeneous reactions were implemented, including dust reactions with O_3, OH, H_2O_2, CH_3COOH, CH_3OH, CH_2O, HNO_3, N_2O_5, NO_2, NO_3, HO_2, and SO_2. The uptake coefficients of gases onto the surface of dust particles were taken from previous published studies in deserts of China. More details of the technical development of this dust emission and chemistry module in CMAQ and the evaluation of model performance can be found in Dong et al. (2015).

The modeling domain includes whole China with a horizontal grid resolution of 36 km×36 km and 34 vertical layers with a model top at 50 hPa. The chemical initial and boundary conditions for CMAQ were downscaled from the GEOS-Chem global model. Emissions inputs included anthropogenic emissions from Zhao et al. (2013) over China, biogenic emissions from MEGAN2.1 (Guenther et al., 2006), and biomass burning emissions from FLAMBE (Reid et al., 2009).

3. Results and Discussion

3.1. Spatiotemporal evolution of the 2010 spring dust storm over China

On March 19, 2010, a super dust storm outbroke over the Gobi Desert of Inner Mongolia, China and southern Mongolia. It was driven by a strong cold front and revealed evidently by the OMI (Ozone Monitoring Instrument) aerosol index (AI) from space detection (Tatarov et al., 2012). Along with the cold front, the dust plumes

moved southeastward, invading extensive areas from Northern China to Southern China. Fig. 2 shows the daily PM_{10} concentrations over 86 cities of China from March 19 to 23, 2010, displaying the spatiotemporal evolution of this dust storm event. On March 20, daily PM_{10} concentrations of higher than 200 μgm^{-3} were observed over widespread areas of Northern China, close to the dust source regions. The PM_{10} concentrations of those heavily polluted cities, including Yinchuan (YC), Datong (DT), Hohhot (HHT), and Beijing (BJ) (red circles in Fig.1a,) reached the threshold of 600 μgm^{-3}, the maximum value recorded by API (Fig. 2a). As the dust plumes transported, high levels of PM_{10} started to emerge over Central and Eastern China on March 21, when heavy pollution with daily PM_{10} concentrations higher than 420μgm^{-3} were observed over the Yangtze River Delta region as well as in Jiangxi, Hunan, and Hubei provinces. Specifically, the PM_{10} concentrations in Shanghai, Nanjing (NJ), Hefei (HF), Wuhan (WH), Hangzhou (HZ), and so on (blue circles in Fig. 1a) all reached the threshold of 600 μgm^{-3} (Fig. 2c). On March 22 and 23, the dust plumes drifted towards Fujian and Guangdong provinces in Southern China, where PM_{10} concentrations of over 600μgm^{-3} were even observed in coastal cities such as Fuzhou (FZ), Xiamen (XM), and Shantou (ST) (pink circles in Fig.1a). The severe air pollution over China caused by this super dust storm lasted for ~4 days until March 23, resulting in significant impacts on the regional air quality and possible perturbation on regional meteorology.

3.2. Identification of two dust plumes with distinct transport pathways

Fig. 3a shows the time-height cross-section of δv (volume depolarization ratio) measured at the wavelength of 532 nm from March 19 to 23 in Shanghai. δv is frequently used to identify dust events and a threshold value of 10% is used to distinguish dust from other types of particles (Shimizu et al., 2004). As shown in Fig. 3a, there were evidently two discontinuous periods with δv higher than 10%, consistent with the two peaks of PM_{10} concentrations measured near the ground (Fig.

281 4c). The first dust episode (DS1) started from ~16:00 LST, March 20 to ~10:00LST,
282 March 21 and the second dust episode (DS2) started from ~6:00 LST, March 22 to
283 ~0:00 LST, March 23.

284 The 48-hours backward trajectories of the air masses during March 20-23 in
285 Shanghai are shown in Fig. 2. It is interesting to note that the transport pathways of
286 the dust plumes in DS1 and DS2 were distinctly different. In DS1, the dust plumes at
287 both low altitudes (i.e. 250m denoted by the black lines in Fig. 2c-d) and high
288 altitudes (i.e. 1000m denoted by the red lines in Fig. 2c-d) were mostly transported
289 from the dust source regions in the Gobi Desert. This is one of the typical inland
290 transport pathways of Asian dust, which passed over Northern China that is
291 characterized of intense anthropogenic emission rates, e.g. from Shanxi, Hebei, and
292 Shandong provinces.

293 In DS2, the air masses reaching Shanghai are shown in Fig. 2e – h. From the
294 starting of DS2 to the midday of March 22 (Fig. 2e-f), the backward trajectories were
295 still mainly from the north but we noticed that the low altitude trajectories which
296 originated from the Gobi Desert travelled over the Yellow Sea and East China Sea
297 and then circled back to Shanghai. After the midday of March 22 (Fig. 2g-h), the
298 trajectories became much shorter and restricted within the costal and offshore areas.
299 The low-altitude trajectories were mainly from the ocean and the high-altitude
300 trajectories shifted from the south. As indicated by the surface observation (Fig. 4a),
301 the southeasterly winds prevailed until ~18:00 LST, March 22 when PM_{10} climbed to
302 reach its peak value in DS2, quite different from DS1 when the northerly winds
303 dominated. The CALIPSO (Cloud-Aerosol Lidar and Infrared Pathfinder Satellite
304 Observations) transect at around 13:00 – 13:30 LST, March 21 specified that the
305 major aerosol type was dust over the East China Sea and South China Sea (Fig. S1).
306 Therefore, it was evident that DS2 passed over the coastal regions of Eastern China
307 and the ocean and it should be a humid dust plume.

308 As visualized in Fig. 3, the two dust plumes were mostly transported at low

altitudes below 1km. It is expected that this type of transport would benefit for the mixing and interactions between dust particles and anthropogenic pollutants, as the anthropogenic emissions were mainly trapped within the boundary layer. Transport pathway is one of the most important factors accounting for the evolution of dust particles and the resulting environmental effects (Zaizen et al., 2014; Zhang et al., 2010). In this super dust storm, the two discontinuous dust plumes reaching Shanghai were distinctly different in their transport pathways, providing a great opportunity to study the chemical evolution of dust particles under different transport conditions.

3.3. Distinct behaviors of gaseous pollutants between two dust episodes

Fig. 4 illustrates the different behaviors of the two identified dust episodes by plotting the temporal variations of emission precursors (i.e. SO_2 and NO_2) as well as PM_{10} and crucial meteorological parameters. As shown in Fig. 4a, the winds prevailed from the south before the onset of DS1 at ~10:00LST, March 20. Starting from early morning of March 19, SO_2 and NO_2 continuously climbed up due to the enhanced human activities. From 18:00 LST of March 19 to 6:00 LST of March 20, the concentrations of NO_2 and SO_2 synchronously decreased. This was partly attributed to the prevailing southeast winds, i.e. sea breezes which had clean effects on the local pollution. Furthermore, the decrease of NO_2 and SO_2 occurred during night, when the anthropogenic emissions were relatively low during a day. During this period, SO_2 and NO_2 concentrations were relatively high with mean concentrations of 39±19 and 70±25μgm-3, respectively. In the meantime, PM_{10} was at a moderate level of 112± 54μgm^{-3}, suggesting the dominance by anthropogenic emissions. It was observed that the peak hourly concentrations of SO_2 and NO_2 up to 97μgm^{-3} and 116μgm^{-3} occurred just a few hours before the sharp increase of PM_{10}. This was due to that air pollutants north of Shanghai were pushed by the cold front and accumulated before the dust plumes invaded (Guo et al., 2004), which was also evident from the time difference between the values of β and δv as shown in Fig. 3.

From 10:00 LST, March 20 to 11:00 LST, March 21, the winds shifted from the north and northwest accompanied with a quick drop of relative humidity (RH) with a minimum of 25% at 21:00 LST, March 20, indicating the invasion of a strong cold front from Northern China. Correspondingly, PM_{10} abruptly climbed since 16:00 LST and reached 1000μgm^{-3} (a maximum value of 1000μgm^{-3} was set in the TEOM 1405D monitor) within four hours. This high level of PM_{10} lasted for ~11 hours till 04:00 LST, March 21. During this dust episode, the concentrations of SO_2 and NO_2 decreased substantially and the lowest values of 17μgm^{-3} and 27μgm^{-3} (Fig. 4c) were recorded at 04:00 LST, March 21, due to the strong dilution effect of dust plumes. The ratios of SO_2/PM_{10} and NO_2/PM_{10} were as low as 0.04±0.02 and 0.06±0.03 in DS1 compared to that of 0.30±0.05 and 0.57±0.28 before DS1. After 12:00 LST, March 21, the wind direction started to shift again from the southeast with an increase of RH. The PM_{10} concentrations quickly decreased below 200 μgm^{-3} within five hours, indicating the pass of the first dust episode over Shanghai.

The second wave of dust (DS2) commenced after about half a day as indicated by the temporal variation of PM_{10} climbing quickly since 6:00 LST, March 22. PM_{10} reached its peak of 530 μgm^{-3} observed at ~18:00LST, March 22, much lower than the peak values during DS1. It should be noted that during the growth of DS2 (i.e. from 06:00 to 18:00 LST), southerly winds sustained until 18:00 LST, March 22, opposite to DS1. As discussed above, DS2 had gone through the maritime environment during most of its transport trajectory. This can be corroborated by the moderately high RH (Fig. 4b). After 18:00 LST, March 22, PM_{10} underwent a quick decline followed by the prevailing northeast winds and continuously elevated RH. This suggested the sea breezes after 18:00 LST were almost free of dust particles and acted as cleaner for the dust pollution that was previously accumulated. Compared to the mean RH of 46% ± 18% in DS1, RH in DS2 was much higher of 69% ± 8%. This was mainly attributed to the different transport pathways of the two dust episodes.

One interesting phenomenon that has been rarely observed was that the temporal

variations of SO_2 and NO_2 varied fairly consistent with that of PM_{10} in DS2 (Fig. 4c), quite different from DS1 and previous studies (Fu et al., 2010; Guo et al., 2004) that dust usually had a clean effect on the local gaseous pollutants, causing inverse relationship between SO_2/NO_2 and PM_{10}. In this case, NO_2 reached its maximum hourly concentration of 131μgm^{-3} along with the maximum PM_{10} in DS2, the highest during the whole study period. This probably indicated that the dust particles in DS2 were externally mixed or "coated" with abundant gaseous pollutants. As a result, the SO_2/PM_{10} and NO_2/PM_{10} ratios reached 0.11 ± 0.03 and 0.20 ± 0.04 in DS2, respectively, much higher than those in DS1 and in a super dust day of April 2, 2007 in Shanghai (Fu et al., 2010), revealing that the dust plumes in DS2 were much more polluted.

In the following sections, we will investigate deeply into the chemical characteristics and evolution of the two dust episodes.

3.4. Chemical evolution of dust particles

3.4.1. Pollution elements significantly enhanced in dust periods

Table 1 lists the concentrations of measured elements in TSP before, during, and after the two dust episodes in Shanghai. D and N represent the samples that collected in daytime (~8:00 to ~20:00 LST) and nighttime (~20:00 to 8:00 LST in the next day), respectively. NDS represents the non-dust days from March 25 to 27 and the mean concentrations are shown in Table 1. To identify whether these elements were mainly derived from the crustal source or anthropogenic sources, enrichment factors of elements were calculated. Enrichment factor (EF) is defined as $EF=(X/X_{Ref})_{particle}/(X/X_{Ref})_{crust}$, where $(X/X_{Ref})_{particle}$ is the mass ratio of a given element X to the reference element in particle and $(X/X_{Ref})_{crust}$ is the ratio in the crust (Lida, 2006), and Al is the reference element used in this study. EFs of Al, Cu, Ca, Fe, Mg, Na, Mn, Ti, Sr, Ni, and V were calculated to be lower than 5, indicating these eleven elements were mostly from the crustal source, while EFs of As, Cd, Pb, and Zn

were higher than 10 even during the dust periods (Fig.5c), indicating these four elements were significantly influenced by anthropogenic sources. Hence, Al, Cu, Ca, Fe, Mg, Na, Mn, Ti, Sr, Ni, and V were classified as "crustal elements" while As, Cd, Pb, and Zn were classified as "pollution elements". Due to the dilution effect of dust plumes, EFs of the four pollution elements decreased from ~100-150 in NDS to ~10-50 in DS1 and ~20-115 in DS2.

As shown in Table 1, the concentrations of the crustal elements before the dust event (19N) were as low as those in NDS, but substantially increased in DS1 and DS2, about 3-13 and 1-7 folds of those in NDS, respectively. The highest concentration of Al, widely used as a tracer for dust, reached 67.5 μgm^{-3} in DS1 (20N), comparable to the Al concentration in the super dust day of April 2, 2007 in Shanghai (Fu et al., 2010). The highest concentrations of crustal elements in DS1 (20N) were ~2 folds of those in DS2 (22D), corroborating that the intensity of DS1 was stronger than in DS2.

As for the pollution elements, the non-crustal part (nc-) of As, Cd, Pb, and Zn were estimated as $nc\text{-}X = X - Al \times (X/Al)_{crust}$. The concentrations of nc-As, nc-Cd, nc-Pb, and nc-Zn increased in both DS1 and DS2, about 1-4folds of those in NDS (Fig. 5a). As these elements were mainly derived from anthropogenic sources such as coal combustion, industrial processing, vehicle emissions, etc., their enhancement indicated that abundant pollutants had been transported to the downwind regions along with the dust plumes. The mean concentrations of nc-As, nc-Cd, nc-Pb, and nc-Zn were 23.5, 3.6, 154.2, and 580.1 ngm^{-3} in DS2, higher than those of 18.3, 3.1, 119.7, and 447.4 ngm^{-3} in DS1, indicating DS2 was more polluted. Consistently, the mass ratios of nc-As, nc-Cd, nc-Pb, and nc-Zn in TSP were 5.1×10^{-3}%, 7.2×10^{-4}%, 3.1×10^{-2}%, and 1.2×10^{-1}% in DS2, higher than those of 1.9×10^{-3}%, 3.7×10^{-4}%, 1.5×10^{-2}%, and 6.2×10^{-2}% in DS1 (Fig. 5b).

3.4.2. Crustal vs. secondary water-soluble ions

Fig. 6 shows the evolution of major water-soluble ions in TSP during the whole

421 dust event. The concentrations of Na^+, K^+, Mg^{2+}, and Ca^{2+} increased the most among
422 all the ions in both DS1 and DS2 due to their crustal origin, ~2-5 and ~2-3 folds of
423 those in NDS. However, the mass ratios of these ions in TSP generally decreased in
424 the dust periods (Fig. 6d), as the masses of dust particles were dominated by
425 water-insoluble matters. Different from NDS, the concentrations of Ca^{2+} exceeded
426 NH_4^+ and ranked as the most abundant cation in the dust periods. This was because
427 Asian dust particles are rich of calcium carbonate (Wang et al., 2005), which could
428 react with acidic nitrogen and sulfur compounds to form $Ca(NO_3)_2$ and $CaSO_4$. It has
429 been found Ca-rich particles in Asian dust transported to Japan were mostly in the
430 spherical shape (Zaizenet al., 2014), and many of the spherical Ca-rich particles
431 contained sulfur and nitrogen compounds (Matsuki et al., 2006; Zaizen et al., 2014)
432 due to the heterogeneous reactions. Recently, Pan et al. (2017) reported that the
433 concentrations of both NO_3^- and Ca^{2+} increased in coarse mode mineral dust in
434 Beijing, particularly at high RH condition due to the interaction between nitric acid
435 and Ca-rich particles. It is further suggested that the impact of nitrate on modifying
436 the morphology of dust particles have become increasingly important, as the NOx
437 emissions in East Asia have been rapidly increasing. It is noted that the concentrations
438 of Ca^{2+} in DS2 were comparable to that in DS1 (Fig. 6b), although the intensity of
439 DS1 was much stronger than DS2. In addition, the mass ratios of Ca^{2+} in TSP were
440 even higher in DS2 than in DS1 (Fig. 6d). Collectively, these results indicated that
441 more calcium in its soluble form was produced via the reactions between calcium
442 carbonate and acids. This could be also revealed by the ratio of Ca^{2+}/Ca that was
443 higher in DS2 (0.2-0.5) than in DS1 (0.1-0.2) (Fig.7a). In DS2, the dust plumes
444 travelled over the ocean and carried higher amount of water vapor as well as SO_2 and
445 NO_2 than DS1 as discussed earlier. In this regard, the heterogeneous reaction between
446 calcium carbonate and acidic gases was enhanced more in DS2, resulting in a higher
447 fraction of calcium carbonate from dust particles that could be transformed to soluble
448 calcium.

449 Cl^- during the dust periods was moderately enhanced by ~1-2 folds compared to
450 NDS, indicating that Cl^- was also impacted by the invasion of dust plumes. As shown
451 in Fig. 6a & 6c, both the concentrations of Cl^- and its mass ratios in TSP were higher
452 in DS2 than in DS1. As the air masses of DS2 passed over the ocean, part of the high
453 Cl^- concentrations should be attributed to the contribution from seasalts. The average
454 equivalent ratio of Cl^- to Na^+ ($[Cl^-]/[Na^+]$) was 1.65 in NDS and 2.17 in 19N, higher
455 than the ratio in seawater (1.17), indicating that anthropogenic sources such as coal
456 combustion (Sun et al., 2014; Yao et al., 2002) contributed significantly to Cl^- in the
457 non-dust days. The $[Cl^-]/[Na^+]$ ratio dropped to ~1.0 in DS1 as massive continental
458 particles invaded Shanghai, while in DS2 the ratio was elevated to 1.5. Thus, both
459 seasalts and anthropogenic sources should contribute to the particulate Cl^- in DS2.
460 As for the secondary inorganic ions (i.e. SO_4^{2-}, NO_3^-, and NH_4^+), their
461 concentrations in TSP were elevated to be 16.2, 15.4, and 7.2μgm^{-3} in the daytime of
462 March 20 (20D) in DS1. The sampling time of 20D was from ~8:00 to 20:00 LST,
463 including the short period of pollutants accumulation before the arrival of DS1. As a
464 result, the high concentrations of SO_4^{2-} and NO_3^- measured in 20D were contributed
465 from both local and transported sulfate and nitrate, as well as from the heterogeneous
466 reactions on dust particles. In the nighttime of March 20 (20N), the concentrations of
467 NO_3^- and NH_4^+ sharply decreased by 57.8% and 43.2%, respectively. Although SO_4^{2-}
468 also decreased, its reduction extent was much weaker of 27.8% and was still ~2 folds
469 of that in NDS (Fig. 6a). Nitrate formation on dust is strongly dependent on the
470 ambient conditions. Low temperature, low relative humidity, strong wind and low
471 concentrations of pollution gases did not favor the heterogeneous reaction (Huang et
472 al., 2010a; Yuan et al., 2008). Hence, strong dust events usually diluted the
473 concentrations of nitrate (Duvall et al., 2008; Huang et al., 2010a; Wang et al., 2006).
474 As for the sulfate formation on dust, SO_2 could interact with various mineral
475 components of dust particles to produce sulfate, and sulfate became mixed with the
476 dust first competing with nitrate (Dupart et al., 2012; Sullivan et al., 2007). Hence,

477 although the secondary particle components were diluted by the invasion of dust, the
478 formation of sulfate could still be compensated by the heterogeneous reaction on dust
479 to some extent.

480 In the daytime of March 22 (22D) during DS2, the concentrations of SO_4^{2-} and
481 NO_3^- reached the highest during the study period with values of 16.6 and 19.3 μgm^{-3},
482 respectively. Although SO_4^{2-} and NO_3^- decreased in the nighttime of March 22 (22N),
483 their levels were still higher than the non-dust days (Fig. 6a). Also, the mass ratios of
484 SO_4^{2-} and NO_3^- in TSP were higher in DS2 than DS1 (Fig. 6c). These results indicated
485 that SO_4^{2-} and NO_3^- were more favorably formed in DS2. It was observed that the
486 concentration of NO_3^- was even higher than that of SO_4^{2-} in both daytime and
487 nighttime samples during DS2, showing a contrary behavior to DS1. As discussed
488 above, the formation of nitrate on dust strongly depends on the ambient conditions.
489 During DS2, RH was at a moderately high level, enhancing the efficiency of aqueous
490 processing on the particles. In addition, the abnormally high concentrations of NO_2
491 (Fig. 4c) suggested the emission precursors were sufficient for the production of
492 nitrate. Finally, high concentrations of nitrate during DS2 may be partially attributed
493 to the reaction between sea salts and nitric acid (Hsu et al., 2014; Huang et al., 2010a)
494 as the dust plumes travelled over the ocean. The formation of secondary aerosol
495 species during DS2 should have involved the complex interactions between pollutant
496 precursors, dust, and sea salts.

497 Fig. 7b shows the equivalent ratio of the total anions to the total cations (A/C) in
498 TSP. The A/C ratio dropped to ~0.5 in DS1 from ~0.9 in 19N, which was attributed to
499 the existence of abundant CO_3^{2-} in dust particles that can't be detected by Ion
500 Chromatography (Huang et al., 2010a). The A/C ratio reached 0.85 and 0.80 in 22D
501 and 22N in DS2, respectively, much higher than those in DS1, suggesting that more
502 fraction of $CaCO_3$ in the dust particles in DS2 was transformed to $CaSO_4$ and
503 $Ca(NO_3)_2$ than in DS1, consistent with the higher Ca^{2+}/Ca ratio in DS2 than in DS1
504 (Fig. 7a). The equivalent ratio of NH_4^+ to the sum of SO_4^{2-} and NO_3^- ($[NH_4^+]$/

505 [SO_4^{2-}+NO_3^-]) in TSP also indicated that the heterogeneous reactions between
506 carbonate and acid gases were more promoted in DS2 compared to DS1. As shown in
507 Fig. 7c, the [NH_4^+]/[SO_4^{2-}+NO_3^-] ratio was slightly higher than one in the non-dust
508 days, indicating that SO_4^{2-} and NO_3^- could be completely neutralized by NH_4^+. In DS1,
509 the [NH_4^+]/[SO_4^{2-}+NO_3^-] ratio was 0.68 and 0.65 in 20D and 20N, while in DS2 it was
510 even lower of 0.45 and 0.55 in 22D and 22N, respectively. Apparently, NH_4^+ was
511 insufficient for completely neutralizing SO_4^{2-} and NO_3^- in both dust episodes,
512 particularly in DS2. The ammonium deficiency was also observed in Kinmen and
513 Zhuhai (Hsu et al., 2014), an island site and a coastal site, respectively, during this
514 super dust storm. We further investigated the [NH_4^++Ca^{2+}+Mg^{2+}]/[SO_4^{2-}+NO_3^-] ratio.
515 As shown in Fig. 7d, with the addition of Ca^{2+} and Mg^{2+}, sulfate and nitrate had been
516 completely neutralized, implying the important role of alkaline calcium and
517 magnesium as the medium of dust heterogeneous reactions. By estimating the
518 neutralization efficiency of Ca^{2+} and Mg^{2+} ($NE_{Ca\&Mg}$) as $NE_{Ca\&Mg}$ = 1 -
519 [NH_4^+]/[SO_4^{2-}+NO_3^-], the average value of $NE_{Ca\&Mg}$ in DS1 and DS2 was 0.34 and
520 0.50, respectively. The higher $NE_{Ca\&Mg}$ in DS2 also suggested the chemical
521 processing via dust was efficient under the environmental conditions such as DS2 in
522 this study.
523
524 **3.5. Vertical evolution of dust particles**
525 In both DS1 and DS2, dust particles were mostly refrained below the altitude of
526 1km. Strong vertical gradients of δv and β were observed (Fig. 3). To quantitatively
527 investigate the evolution of vertical dust profiles, we selected four typical episodes as
528 follows: 1. 9:00-15:00 LST of March 20: an episode right before the arrival of DS1; 2.
529 16:00 - 17:45 LST of March 20: an episode before the onset of maximum hourly
530 PM_{10} concentrations in DS1; 3. 18:00 LST of March 20 - 4:45 LST of March 21, an
531 episode that covers the highest PM_{10} concentrations hours (>1000μgm^{-3}) in DS1; 4.
532 6:00 - 18:00 LST of March 22: an episode in DS2.

As shown in Fig. 8a, the mean σ between 9:00 - 15:00LST, March 20 ranged from around 0.12 to 0.72 km^{-1} from near ground level to 1km. During this period, the mean δp was relatively low of ~ 0.02 - 0.08, suggesting spherical particles, i.e. pollution particles dominated. Accordingly, the contribution of dust to the total particle extinction (dust ratio) was less than 20% (Fig. 8e). As discussed earlier, the high values of light extinction caused by pollution particles before the onset of DS1 were due to the pre-accumulation of local and transported pollutants brought by the invaded cold front. On the pathway of DS1 (Fig. 2c), the air masses travelled over large areas with intense anthropogenic emissions and thus a large quantity of pollutants could be pushed to the downstream areas and accumulated before the dust plume arrived.

As DS1 invaded, the mean σ further increased and reached 0.73 km^{-1} near the surface level (Fig. 8b-c). In the meantime, the values of δp were elevated to be higher than 10% from near the ground to ~ 1km (Fig.8f-g). When PM_{10} reached its highest concentrations (>1000μgm^{-3}), the mean δp was ~23-27% extending from near the ground to ~700m (Fig.8g). However, compared to the δp value of ~30–35% for the relatively pure Asian dust (Murayama et al., 2003; Sakai et al., 2003), the δp in DS1 was still lower, suggesting the mixing of dust with pollution at a certain extent. As shown in Fig. 8b-c, the mean σ_d obviously overwhelmed the mean σ_s and could be up to 0.82 km^{-1} near the surface level, while the mean σ_s dropped to less than 0.1 km^{-1}. From near the ground to ~700m, no significant vertical gradients of δp and dust ratio were observed. This indicated DS1 had a “top-down” effect on modifying the bulk particle optical properties in the lower troposphere in this case. Within this altitude range, dust could account for ~ 80 - 90% of the total particle extinction coefficients while only a minor fraction of ~10 - 20% was attributed to the pollution particles. Above 700m, δp and the dust ratio quickly deceased, suggesting the impact of dust on the light extinction was much weakened.

In DS2, the maximum σ and δp averaged between 6:00 and 18:00 LST, March 22 was ~0.61km^{-1} and 26%, respectively, observed at an altitude of ~300m. Different

561 from DS1, both δp and the dust ratio had a significant vertical gradient in DS2. As
562 showed in Fig. 8h, δp decreased quickly from its maximum value at ~250m to 5% at
563 ~750m. Correspondingly, the dust ratios decreased from 88% to 25%. Moreover, the
564 vertical profiles of σ_d and σ_s showed distinctly different behaviors during this period.
565 As shown in Fig. 8d, the maximum σ_d (~0.55 km^{-1}) showed at the altitude of ~250m,
566 while that of σ_s (~0.25km^{-1}) appeared at a higher altitude of ~800m. As compared to
567 DS1 (Fig. 8b-c), the σ_s in DS2 showed similar magnitudes below ~ 270m. Above this
568 altitude, the σ_s in DS2 gradually increased while that in DS1 varied relatively stable
569 with the altitudes. The enhancement of pollution particles in the middle layer during
570 DS2 should be mainly attributed to its unique transport pathway. As shown in Fig. 2e,
571 substantial air masses in the upper layer transported from the south and may bring
572 more moisture. The sounding data at a meteorology station (31.40°N, 121.46°E) in
573 Shanghai supported this statement as shown in Fig. S2.
574 Opposite to the low relative humidity (RH) and its decreasing trend with altitude in
575 DS1, RH in DS2 (measured at 8:00 and 20:00 LST of March 22, respectively) showed
576 much higher values and an increasing trend with altitude (Fig. S2). This phenomenon
577 corroborated our discussions above that the meteorological conditions were more
578 favorable for promoting the dust chemistry in DS2. As a result, the secondary aerosol
579 formation via heterogeneous reaction yielded stronger particle extinction in DS2,
580 especially in the middle and upper layers through 270m till the top (2km) where the
581 particle extinctions caused by spherical particles were still significant. On the other
582 hand, due to the higher humidity in DS2, the soluble particle components should
583 undergo stronger hygroscopic growth and thus partly explain the structure of vertical
584 profile of spherical particles as shown in Fig. 8d. It is commonly regarded that in a
585 dry and less oxidative environment that dust storms are usually associated with, the
586 formation and growth of secondary particles are often depressed. However, under
587 certain favorable conditions, new particle formation during dust events could be still
588 discernible (Nie et al., 2014). In this study, vertical profiles of crucial meteorological

parameters, pollutant precursors and particle numbers were not available for diagnosing the new particle formation. Tethered balloon-based measurement (Li et al., 2015) could be a good platform for investigating the particle formation during dust events at different altitudes in the future research.

3.6 Impact of dust chemistry on regional air quality

Chemical transport modeling (Methods in Section 2.5) was utilized to assess the impact of dust chemistry on the perturbation of air quality at the regional scale. The model performance of CMAQ with improved dust module has been evaluated against various observational datasets and it was demonstrated that the model has relatively good capability in capturing both magnitudes and temporal variability of bulk aerosol (e.g. PM_{10}, AOD) during the spring season over China (Dong et al., 2016). It has to be noted that the model only simulated the particle size up to 10 μm while the observation of particle chemistry included all the sizes (i.e. TSP), hence the mismatch of size distribution between the model and observation precluded the evaluation of the simulated particle chemical species in this study. In the following discussions, we focused on the qualitative assessment of the impact of dust chemistry on the regional air quality.

Fig. 9 shows the spatial distribution of simulated mineral particles from March 20 – 22, 2010, respectively. Accordingly, we show the spatial distribution of Ultraviolet Aerosol Index (UVAI) retrieved from OMI during the same period. UVAI is sensitive to absorbing particles, i.e. black carbon and mineral dust (Torres et al., 2007). Hence, the comparison between simulated mineral particles and observed UVAI could illustrate how the transport of dust was reproduced. However, based on the definition of Aerosol Index, it is a parameter based on the difference between radiance at two near ultraviolet wavelengths. Thus, the comparison between satellite Aerosol Index and simulated mineral dust is only qualitative. As seen from Fig. 9, high values of UVAI were always observed over the Indo-China Peninsula and this was ascribed to

617 the black carbon particles emitted from strong biomass burning over this region
618 during the spring season (Fu et al., 2012; Huang et al., 2013; Tsay et al., 2013). What
619 we concern are the dust and its downwind regions over East Asia. On March 20, high
620 UVAI values stretched from the Gobi Desert to the North China Plain and the Yangtze
621 River Delta. This transport pathway was relatively well reproduced by the model as
622 we can see high concentrations of mineral particles over similar areas as well. On the
623 following day of March 21, the satellite observation illustrated the movement of the
624 high UVAI zones further southward and the drifting of dust plumes off the coastline
625 of East China (Fig. 9c). Accordingly, the simulation showed similar behavior with
626 strengthened concentrations of mineral particles over the Gobi Desert and downwind
627 areas of the Yangtze River Delta (Fig. 9d). On March 22, although UVAI signals were
628 absent over most areas of East China due to the satellite swath, high UVAI values
629 could still be observed over the tip of the Yangtze River Delta and the East China Sea.
630 This is also relatively consistent with the model simulation that high concentrations of
631 mineral particles hovered over the coastlines from YRD to the Taiwan Strait. Overall,
632 we demonstrated that the model is capable of capturing the spatial distribution of dust
633 during the long-range transport.
634 Since we specifically focus on the interaction between dust and anthropogenic
635 pollutants in this study, we have performed two simulations, i.e. one with dust
636 emissions but without dust chemistry and the other one with dust chemistry. The
637 impact of dust chemistry on particle chemical components could thus be quantified
638 via the difference between these two simulations. Fig. 10a&c shows the spatial
639 distribution of sulfate via the formation pathway of dust heterogeneous reactions, as
640 well as for nitrate in Fig. 10b&d. Different from the spatial distribution of mineral
641 particles (Fig. 9a-c), the formation of sulfate and nitrate via dust chemistry mainly
642 occurred over Northeastern China. This is expected that although the major source
643 region of mineral dust is from the Gobi Desert in Northern China, less anthropogenic
644 emission sources existed there, hence relatively weak atmospheric chemical

processing was simulated over the dust source region. On the other hand, drier climate in Northern China also suppressed the extent of heterogeneous reactions on the surface of dust. Hence, the strongest impact from dust heterogeneous reactions on the formation of secondary particles occurred in those populous areas where the interaction of anthropogenic precursors and dust was the strongest.

As for sulfate, the simulated concentration over Shanghai averaged 8.1, 3.1, and 8.5 μgm^{-3} from March 20 – 22, respectively. This temporal variation corresponded to that from observation as discussed in Section 3.4.2. While it has to be noted again that the simulated particle species contained particulate sizes less than 10 μm, close match between the simulation and observation was not expected. As we compare DS1 (Fig. 10a) and DS2 (Fig. 10c), the simulated sulfate during DS2 was evidently more intense than that during DS1 at a larger geographic region, which was fairly consistent with the observation. Since the daily emission rates digested by the model were almost constant during this period, meteorological conditions should be the determining factor, of which elevated humidity during DS2 has been diagnosed as the most important factor responsible for stronger dust chemistry.

As for nitrate, its spatial distribution pattern was as similar as that of sulfate at a certain extent. The simulated concentration of nitrate averaged 3.1, 2.3, and 5.2 μgm^{-3} over Shanghai from March 20 – 22, respectively. Although the simulation results and observational data couldn't be statistically inter-compared due to the size difference as stated above, we think the simulated nitrate should be largely underestimated. The ratio of simulated nitrate between DS2 and DS1 was 1.7, similar to that of ~1.6 from observation. This suggested the favorable meteorological conditions (e.g. higher humidity) on facilitating the dust heterogeneous reaction during DS2 have been accounted by the model. In this regard, we ascribe the low- biased nitrate mainly to several aspects. First, the NOx emissions could have been underestimated. As indicated in Dong et al. (2015) which used the same anthropogenic emission inventory as this study, the model showed some underestimation of the total NO_2

673 columns as compared to the OMI observation, especially over Northeastern China
674 (See Fig. 8 in Dong et al.(2015)). Secondly, HNO_3, N_2O_5, NO_2 and NO_3 were the
675 major precursors of nitrate as implemented in the dust module. Of which, reactions
676 via HNO_3 and N_2O_5 were the dominant pathways of nitrate formation due to their
677 relatively high uptake coefficients on the dust. It was possible that the formation of
678 HNO_3 was underestimated, thus lowering the production of nitrate. However, this is
679 just a guess as observation of gaseous HNO_3 was not available in this study. Lastly,
680 we think the underestimation of nitrate may be due to the omission of nitrate
681 processing on the surface of sea salt, which was especially important for costal cities
682 such as Shanghai (Buseck and Posfai, 1999).
683
684
685 **4. Conclusions**
686 During March 19-23, 2010, a super dust storm swept extensive areas over China
687 from Northern China to Southern China. Two separate dust periods were observed in
688 Shanghai, one from ~16:00 LST, March 20 to ~10:00 LST March 21 (DS1) and the
689 other from ~6:00 LST, March 22 to ~0:00 LST, March 23 (DS2). In DS1, the dust
690 plumes mostly transported over those areas characterized of high pollution emissions
691 in Northern China, while the dust plumes in DS2 transported over the coastal regions
692 of Eastern China with higher RH. The ratios of SO_2/PM_{10} and NO_2/PM_{10} were up to
693 0.11 ± 0.03 and 0.20 ± 0.04 in DS2, much higher than the values in DS1. In addition,
694 the concentrations of typical elemental species such as As, Cd, Pb, and Zn were also
695 more enriched in DS2 than in DS1, indicating the stronger mixing extent between dust
696 and primary anthropogenic emissions in DS2. Due to the higher level of gaseous
697 pollutant precursors associated with moderate relative humidity, SO_4^{2-} and NO_3^-
698 exhibited higher concentrations in DS2 than in DS1. The higher Ca^{2+}/Ca ratio and
699 lower $[NH_4^+]/[SO_4^{2-}+NO_3^-]$ ratio in DS2 suggested the heterogeneous reactions
700 between calcites and acid gases were significantly promoted in DS2. Particularly,
701 more NO_3^- than SO_4^{2-} was formed in DS2, probably due to the high concentrations of

NO_2 and the complex reaction among dust, seasalts, and nitric acid. Vertical profiles of particle optical properties from Lidar measurement retrieved high depolarization ratios of 20-25% extending from near the ground to ~700m in DS1 and it was estimated that dust dominantly accounted for ~80-90% of the total particle extinction. In DS2, the vertical structure of particles changed dramatically from that of DS1. The maximum extinction coefficient of dust particles emerged at the altitude of ~250m in DS2, while that of pollution particles showed at a higher altitude of ~800m. The abnormal increase of humidity as a function of altitude from the southerly winds explained this phenomenon due to promoted heterogeneous reactions on dust particles and the subsequent particle hygroscopic growth.

Simulated mineral particles were compared to the remote sensing UVAI from satellite, showing consistent spatial patterns between model and observation. By applying the dust scheme with explicit chemistry mechanisms, evident impacts of dust heterogeneous reactions on secondary aerosol formation were reproduced over widespread areas of Northeastern China where the anthropogenic emissions were intensive. The sulfate formation was relatively well simulated while the nitrate formation on dust was believed to be largely underestimated. More research on laboratory kinetic studies of nitrate dust chemistry is suggested. Also, the feedback between dust chemistry and regional climate change needs to be investigated in the future.

Acknowledgment

This work was supported by the National Natural Science Foundation of China (Nos. 41405115, 41429501, and 91644105) and National Key Technology Research and Development Program of the Ministry of Science and Technology of China (No. 2014BAC22B06). Dr. Qingyan Fu and Yanfen Lin would like to acknowledge support from Shanghai Science and Technology Fund (Nos. 14DZ1202900 and 16DZ1204601) and National Key Technology Research and Development Program of the Ministry of

730 Science and Technology of China (No. 2014BAC22B00).

731

732 **References:**

733 Bi, J., Huang, J., Holben, B., 2016. Comparison of key absorption and optical
734 properties between pure and transported anthropogenic dust over East and Central
735 Asia. 1-37.
736 Bi, J., Shi, J., Xie, Y., 2014. Dust Aerosol Characteristics and Shortwave Radiative
737 Impact at a Gobi Desert of Northwest China during the Spring of 2012. Journal of the
738 Meteorological Society of Japan 92, 33-56.
739 Buseck, P., Posfai, M., 1999. Airborne minerals and related aerosol particles: Effects
740 on climate and the environment. Proc. Natl. Acad. Sci. U. S. A., 3372–3379, doi:
741 10.1073/pnas.96.7.3372.
742 Chen S., J. Huang, L. Kang, H. Wang, X. Ma, Y. He, T. Yuan, B. Yang, Z. Huang,
743 and G. Zhang (2017). Emission, transport and radiative effects of mineral dust from
744 Taklimakan and Gobi Deserts: comparison of measurements and model results.
745 Atmospheric Chemistry and Physics,17(3):1-43, doi: 10.5194/acp-17-2401-2017.
746 Creamean, J.M., Suski, K.J., Rosenfeld, D., Cazorla, A., Demott, P.J., Sullivan, R.C.,
747 White, A.B., Ralph, F.M., Minnis, P., Comstock, J.M., 2013. Dust and biological
748 aerosols from the Sahara and Asia influence precipitation in the western U.S. Science
749 339, 1572.
750 Dong, X., Fu, J.S., Huang, K., Tong, D., Zhuang, G., 2015. Model development of
751 dust emission and heterogeneous chemistry within the Community Multiscale Air
752 Quality modeling system and its application over East Asia. Atmospheric Chemistry
753 & Physics 15, 35591-35643.
754 Dupart, Y., King, S.M., Nekat, B., Nowak, A., Wiedensohler, A., Herrmann, H., David,
755 G., Thomas, B., Miffre, A., Rairoux, P., 2012. Mineral dust photochemistry induces
756 nucleation events in the presence of SO2. Proc Natl Acad Sci U S A 109,
757 20842-20847.
758 Duvall, R.M., Majestic, B.J., Shafer, M.M., Chuang, P.Y., Simoneit, B.R.T., Schauer,
759 J.J., 2008. The water-soluble fraction of carbon, sulfur, and crustal elements in Asian
760 aerosols and Asian soils. Atmospheric Environment 42, 5872-5884.
761 Eguchi, K., I. Uno, K. Yumimoto, et al., 2009: Trans-pacific dust transport: integrated
762 analysis of NASA/CALIPSO and a global aerosol transport model. Atmos. Chem.
763 Phys., 9, 3137-3145.
764 Fernald, F.G., 1984. Analysis of atmospheric lidar observations: some comments.
765 Applied Optics 23, 652.
766 Fischer, E.V., Perry, K.D., Jaffe, D.A., 2011. Optical and chemical properties of
767 aerosols transported to Mount Bachelor during spring 2010. Journal of Geophysical
768 Research-Atmospheres 116, 13.
769 Formenti, P., Schutz, L., Balkanski, Y., Desboeufs, K., Ebert, M., Kandler, K., Petzold,
770 A., Scheuvens, D., Weinbruch, S., Zhang, D., 2011. Recent progress in understanding

771 physical and chemical properties of African and Asian mineral dust. Atmospheric
772 Chemistry and Physics 11, 8231-8256.
773 Fu, J.S., Hsu, N.C., Gao, Y., Huang, K., Li, C., Lin, N.H., Tsay, S.C., 2012. Evaluating
774 the influences of biomass burning during 2006 BASE-ASIA: a regional chemical
775 transport modeling. Atmospheric Chemistry & Physics 12, 5271-5273.
776 Fu, Q.Y., Zhuang, G.S., Li, J.A., Huang, K., Wang, Q.Z., Zhang, R., Fu, J., Lu, T.,
777 Chen, M., Wang, Q.A., Chen, Y., Xu, C., Hou, B., 2010. Source, long-range transport,
778 and characteristics of a heavy dust pollution event in Shanghai. Journal of
779 Geophysical Research-Atmospheres 115, -.
780 Fu,X., S. X. Wang, Z. Cheng, J. Xing, B. Zhao , J. D. Wang, and J. M. Hao, 2014:
781 Source, transport and impacts of a heavy dust event in the Yangtze River Delta, China,
782 in 2011. Atmos. Chem. Phys., 14, 1239–1254.
783 Guenther, A., Karl, T., Harley, P., Wiedinmyer, C., Palmer, P.I., Geron, C., 2006.
784 Estimates of global terrestrial isoprene emissions using MEGAN (Model of Emissions
785 of Gases and Aerosols from Nature). Atmospheric Chemistry & Physics 6, 3181-3210.
786 Guo, J., Rahn, K.A., Zhuang, G.S., 2004. A mechanism for the increase of pollution
787 elements in dust storms in Beijing. Atmospheric Environment 38, 855-862.
788 Hsu, S.-C., Lee, C.S.L., Huh, C.-A., Shaheen, R., Lin, F.-J., Liu, S.C., Liang, M.-C.,
789 Tao, J., 2014. Ammonium deficiency caused by heterogeneous reactions during a
790 super Asian dust episode. Journal of Geophysical Research: Atmospheres 119,
791 2013JD021096.
792 Huang J., T. Wang, W. Wang, Z. Li, and H. Yan, 2014: Climate effects of dust
793 aerosols over East Asian arid and semiarid regions. J. Geophys. Res.: Atmospheres,
794 119, 11398-11416.
795 Huang, K., Fu, J.S., Hsu, N.C., Gao, Y., Dong, X., Tsay, S.C., Yun, F.L., 2013. Impact
796 assessment of biomass burning on air quality in Southeast and East Asia during
797 BASE-ASIA. Atmospheric Environment 78, 291-302.
798 Huang, K., Zhuang, G., Lin, Y., Fu, J.S., Wang, Q., Liu, T., Zhang, R., Jiang, Y., Deng,
799 C., Fu, Q., Hsu, N.C., Cao, B., 2012. Typical types and formation mechanisms of haze
800 in an Eastern Asia megacity, Shanghai. Atmos. Chem. Phys. 12, 105-124.
801 Huang, K., Zhuang, G.S., Li, J.A., Wang, Q.Z., Sun, Y.L., Lin, Y.F., Fu, J.S., 2010a.
802 Mixing of Asian dust with pollution aerosol and the transformation of aerosol
803 components during the dust storm over China in spring 2007. Journal of Geophysical
804 Research-Atmospheres 115, -.
805 Huang, K., Zhuang, G.S., Lin, Y.F., Li, J.A., Sun, Y.L., Zhang, W.J., Fu, J.S., 2010b.
806 Relation between optical and chemical properties of dust aerosol over Beijing, China.
807 Journal of Geophysical Research-Atmospheres 115, -.
808 IPCC, 2013. Climate Change 2013: The Physical Science Basiss, Contribution of
809 Working Group I to the Fifth Assessment Report of the Intergovernmental Panel on
810 Climate Change. Cambridge University Press, New York, USA.
811 Li, J., Fu, Q., Huo, J., Wang, D., Yang, W., Bian, Q., Duan, Y., Zhang, Y., Pan, J., Lin,
812 Y., Huang, K., Bai, Z., Wang, S.-H., Fu, J.S., Louie, P.K.K., 2015. Tethered

balloon-based black carbon profiles within the lower troposphere of Shanghai in the 2013 East China smog. Atmospheric Environment 123, Part B, 327-338.
Li, J.W., Han, Z.W., Zhang, R.J., 2011. Model study of atmospheric particulates during dust storm period in March 2010 over East Asia. Atmospheric Environment 45, 3954-3964.
Li, R., Min, Q.L., 2010. Impacts of mineral dust on the vertical structure of precipitation. Journal of Geophysical Research-Atmospheres 115, 14.
Lida, D.R., 2006. Handbook of Chemistry and Physics: A Ready-Reference Book of Chemical and Physical Data. 86th ed. CRC Press, New York, 14-17.
Liu, Z.Y., Sugimoto, N., Murayama, T., 2002. Extinction-to-backscatter ratio of Asian dust observed with high-spectral-resolution lidar and Raman lidar. Applied Optics 41, 2760-2767.
Matsuki, A., Iwasaka, Y., Shi, G., Zhang, D., Trochkine, D., Yamada, M., Kim, Y.S., Chen, B., Nagatani, T., Miyazawa, T., 2006. Morphological and chemical modification of mineral dust: Observational insight into the heterogeneous uptake of acidic gases. Geophysical Research Letters 32, 312-329.
Murayama, T., Masonis, S.J., Redemann, J., Anderson, T.L., Schmid, B., Livingston, J.M., Russell, P.B., Huebert, B., Howell, S.G., Mcnaughton, C.S., 2003. An intercomparison of lidar-derived aerosol optical properties with airborne measurements near Tokyo during ACE-Asia. Journal of Geophysical Research Atmospheres 108, 8561.
Nie, W., Ding, A., Wang, T., Kerminen, V.-M., George, C., Xue, L., Wang, W., Zhang, Q., Petäjä, T., Qi, X., Gao, X., Wang, X., Yang, X., Fu, C., Kulmala, M., 2014. Polluted dust promotes new particle formation and growth. Scientific Reports, 4(2), 6634.
Pan, X., Uno, I., Zhe, W., Nishizawa, T., Sugimoto, N., Yamamoto, S., Yamamoto, S., Kobayashi, H., Sun, Y., Fu, P., Tang, X., and Wang Z., 2017. Real-time observational evidence of changing asian dust morphology with the mixing of heavy anthropogenic pollution. Scientific Reports, 7(1), 335.
Reid, J.S., Hyer, E.J., Prins, E.M., Westphal, D.L., Zhang, J., Wang, J., Christopher, S.A., Curtis, C.A., Schmidt, C.C., Eleuterio, D.P., 2009. Global Monitoring and Forecasting of Biomass-Burning Smoke: Description of and Lessons From the Fire Locating and Modeling of Burning Emissions (FLAMBE) Program. IEEE Journal of Selected Topics in Applied Earth Observations & Remote Sensing 2, 144-162.
Sakai, T., Nagai T., Nakazato M., Mano Y., and Matsumura T., 2003. Ice clouds and Asian dust studied with lidar measurements of particle extinction-to-backscatter ratio, particle depolarization, and water-vapor mixing ratio over Tsukuba, Applied Optics 42, 7103–7116.
Shimizu, A., Sugimoto, N., Matsui, I., Arao, K., Uno, I., Murayama, T., Kagawa, N., Aoki, K., Uchiyama, A., Yamazaki, A., 2004. Continuous observations of Asian dust and other aerosols by polarization lidars in China and Japan during ACE-Asia. Journal of Geophysical Research: Atmospheres 109, D19S17.

Shimizu, A., Nishizawa, T., Jin, Y., Kim, S. W., Wang, Z., Batdorj, D., Sugimoto, N., 2017. Evolution of a lidar network for tropospheric aerosol detection in east asia. Optical Engineering, 56(3), 031219.
Sugimoto, N., Matsui, I., Shimizu, A., Uno, I., Asai, K., Endoh, T., Nakajima, T., 2002. Observation of dust and anthropogenic aerosol plumes in the Northwest Pacific with a two-wavelength polarization lidar on board the research vessel Mirai. Geophysical Research Letters 29.
Sullivan, R.C., Guazzotti, S.A., Sodeman, D.A., Prather, K.A., 2007. Direct observations of the atmospheric processing of Asian mineral dust. Atmospheric Chemistry & Physics 7, 1213-1236.
Sun, Y.L., Jiang, Q., Wang, Z.F., Fu, P.Q., Li, J., Yang, T., Yin, Y., 2014. Investigation of the sources and evolution processes of severe haze pollution in Beijing in January 2013. J Geophys Res-Atmos 119, 4380-4398.
Sun, Y.L., Zhuang, G.S., Huang, K., Li, J.A., Wang, Q.Z., Wang, Y., Lin, Y.F., Fu, J.S., Zhang, W.J., Tang, A.H., Zhao, X.J., 2010. Asian dust over northern China and its impact on the downstream aerosol chemistry in 2004. Journal of Geophysical Research-Atmospheres 115, -.
Sun, Y.L., Zhuang, G.S., Ying, W., Han, L.H., Guo, J.H., Mo, D., Zhang, W.J., Wang, Z.F., Hao, Z.P., 2004. The air-borne particulate pollution in Beijing - concentration, composition, distribution and sources. Atmospheric Environment 38, 5991-6004.
Tatarov, B., Muller, D., Noh, Y.M., Lee, K.H., Shin, D.H., Shin, S.K., Sugimoto, N., Seifert, P., Kim, Y.J., 2012. Record heavy mineral dust outbreaks over Korea in 2010: Two cases observed with multiwavelength aerosol/depolarization/Raman-quartz lidar. Geophysical Research Letters 39, 5.
Tobo, Y., Zhang, D.Z., Matsuki, A., Iwasaka, Y., 2010. Asian dust particles converted into aqueous droplets under remote marine atmospheric conditions. Proc. Natl. Acad. Sci. U. S. A. 107, 17905-17910.
Torres, O., Tanskanen, A., Veihelmann, B., Ahn, C., Braak, R., Bhartia, P.K., Veefkind, P., Levelt, P., 2007. Aerosols and surface UV products from Ozone Monitoring Instrument observations: An overview. J Geophys Res-Atmos 112.
Tsai, J-H T,Huang K-L, Lin, N-H, Chen, S-J, Lin, T-Chang, Chen, S-C, Lin, C.-C., Hsu, S.-C., Lin, W.-Y., 2012. Influence of an Asian Dust Storm and Southeast Asian Biomass Burning on the Characteristics of Seashore Atmospheric Aerosols in Southern Taiwan. Aerosol & Air Quality Research 12, 1105-1115.
Tsai, F., Tu, J.-Y., Hsu, S.-C., Chen, W.-N., 2014. Case study of the Asian dust and pollutant event in spring 2006: Source, transport, and contribution to Taiwan. Science of the Total Environment 478, 163-174.
Tsai, F.J., Fang, Y.S., Huang, S.J., 2013. CASE STUDY OF ASIAN DUST EVENT ON MARCH 19-25, 2010 AND ITS IMPACT ON THE MARGINAL SEA OF CHINA. J. Mar. Sci. Technol.-Taiwan 21, 353-360.
Tsay, S.C., Hsu, N.C., Lau, K.M., Li, C., Gabriel, P.M., Ji, Q., Holben, B.N., Welton, E.J., Nguyen, A.X., Janjai, S., 2013. From BASE-ASIA toward 7-SEAS: A

satellite-surface perspective of boreal spring biomass-burning aerosols and clouds in Southeast Asia. Atmospheric Environment 78, 20-34.
Uchiyama, A., Yamazaki, A., Togawa, H., Asano, J., Shi, G., 2005. Single Scattering Albedo of Aeolian Dust as Inferred from Sky-radiometer and in situ Ground-based Measurement. Scientific Online Letters on the Atmosphere Sola 1, 209-212.
Uno, I., Eguchi, K., Yumimoto, K., Takemura, T., Shimizu, A., Uematsu, M., Liu, Z.Y., Wang, Z.F., Hara, Y., Sugimoto, N., 2009. Asian dust transported one full circuit around the globe. Nature Geoscience 2, 557-560.
Wang, S.-H., Hsu, N.C., Tsay, S.-C., Lin, N.-H., Sayer, A.M., Huang, S.-J., Lau, W.K.M., 2012. Can Asian dust trigger phytoplankton blooms in the oligotrophic northern South China Sea? Geophysical Research Letters 39, L05811.
Wang, S.H., Lin, N.H., OuYang, C.F., Wang, J.L., Campbell, J.R., Peng, C.M., Lee, C.T., Sheu, G.R., Tsay, S.C., 2010. Impact of Asian dust and continental pollutants on cloud chemistry observed in northern Taiwan during the experimental period of ABC/EAREX 2005. Journal of Geophysical Research-Atmospheres 115, -.
Wang, S.H., Tsay, S.C., Lin, N.H., Hsu, N.C., Bell, S.W., Li, C., Ji, Q., Jeong, M.J., Hansell, R.A., Welton, E.J., Holben, B.N., Sheu, G.R., Chu, Y.C., Chang, S.C., Liu, J.J., Chiang, W.L., 2011. First detailed observations of long-range transported dust over the northern South China Sea. Atmospheric Environment 45, 4804-4808.
Wang, Y., Zhuang, G.S., Sun, Y., An, Z.S., 2005. Water-soluble part of the aerosol in the dust storm season - evidence of the mixing between mineral and pollution aerosols. Atmospheric Environment 39, 7020-7029.
Wang, Y., Zhuang, G.S., Sun, Y.L., An, Z.S., 2006. The variation of characteristics and formation mechanisms of aerosols in dust, haze, and clear days in Beijing. Atmospheric Environment 40, 6579-6591.
Wu, Y., Han, Z., Nazmi, C., Gross, B., Moshary, F., 2015. A trans-Pacific Asian dust episode and its impacts to air quality in the east coast of U.S. Atmospheric Environment 106, 358-368.
Yao, X., Chan, C.K., Fang, M., Cadle, S., Chan, T., Mulawa, P., He, K., Ye, B., 2002. The water-soluble ionic composition of PM2.5 in Shanghai and Beijing, China. Atmospheric Environment 36, 4223-4234.
Yuan, H., Wang, Y., Zhuang, G., 2003. The simultaneous determination of organic acid, MSA with inorganic anions in aerosol and rainwater by ion chromatography (in Chinese). Journal of Instrument Analalysis 6, 6-12.
Yuan, H., Zhuang, G.S., Li, J., Wang, Z.F., Li, J., 2008. Mixing of mineral with pollution aerosols in dust season in Beijing: Revealed by source apportionment study. Atmospheric Environment 42, 2141-2157.
Zaizen, Y., Naoe, H., Takahashi, H., Okada, K., 2014. Modification of Asian-dust particles transported by different routes – A case study. Atmospheric Environment 97, 435-446.
Zhang, W.J., Zhuang, G.S., Huang, K., Li, J.A., Zhang, R., Wang, Q.Z., Sun, Y.L., Fu, J.S., Chen, Y., Xu, D.Q., Wang, W., 2010. Mixing and transformation of Asian dust

with pollution in the two dust storms over the northern China in 2006. Atmospheric Environment 44, 3394-3403.
Zhao, B., Wang, S., Dong, X., Wang, J., Duan, L., Fu, X., Hao, J., Fu, J., 2013. Environmental effects of the recent emission changes in China: implications for particulate matter pollution and soil acidification. Environmental Research Letters 8, 024031.
Zhao, J., Zhang, F., Xu, Y., Chen, J., Yin, L., Shang, X., Xu, L., 2011. Chemical Characteristics of Particulate Matter during a Heavy Dust Episode in a Coastal City, Xiamen, 2010. Aerosol & Air Quality Research 11, 300-309.
Zhao, T.L., S. L. Gong, X. Y. Zhang, et al., 2006: A Simulated Climatology of Asian Dust Aerosol and Its Trans-Pacific Transport. Part I: Mean Climate and Validation. J. Climate., 19,88–103. doi: http://dx.doi.org/10.1175/JCLI3605.1.
Zhuang, G.S., Guo, J.H., Yuan, H., Zhao, X.J., 2001. The compositions, sources, and size distribution of the dust storm from China in spring of 2000 and its impact on the global environment. Chinese Science Bulletin 46, 895-901.
Zhuang, G.S., Yi, Z., Duce, R.A., Brown, P.R., 1992. Link between Iron and Sulfur Cycles Suggested by Detection of Fe(Ii) in Remote Marine Aerosols. Nature 355, 537-539.

957 Table 1 Concentrations of the measured elements (μg/m^3) in TSP before, during, and
958 after the dust periods from March 19 to 22 and in non-dust days (NDS) in Shanghai.
959 N, D, and NDS represent the nighttime samples collected from 20:00 to 8:00 in the
960 next day, the daytime samples collected from 8:00 to 20:00, and the average of the
961 non-dust samples collected from March 25 to 27, respectively.

962

		DS1				DS2		
	19 N	20 D	20 N	21 D	21 N	22 D	22 N	NDS
TSP	168.5	605.0	1306.7	155.1	194.3	683.3	348.2	160.5
Al	6.2	36.4	67.5	9.6	9.3	35.8	12.8	5.2
Ca	8.5	37.3	56.9	9.4	8.6	33.2	12.0	8.0
Fe	3.2	23.3	42.1	6.8	6.0	23.7	11.6	4.2
Mg	1.4	9.5	14.4	2.2	2.3	8.1	3.4	1.4
Na	1.3	7.9	19.1	2.8	3.9	7.9	3.5	2.4
Mn	0.2	1.0	2.2	0.4	0.3	1.1	0.6	0.2
Ti	0.2	1.9	4.3	0.6	0.5	1.9	0.7	0.3
Sr	4.3×10^{-2}	1.6×10^{-1}	3.3×10^{-1}	4.8×10^{-2}	4.3×10^{-2}	1.9×10^{-1}	6.4×10^{-2}	3.8×10^{-2}
V	1.5×10^{-2}	5.2×10^{-2}	1.0×10^{-1}	1.7×10^{-2}	1.5×10^{-2}	4.7×10^{-2}	2.7×10^{-2}	1.3×10^{-2}
Ni	6.7×10^{-3}	2.5×10^{-2}	4.6×10^{-2}	1.1×10^{-2}	3.0×10^{-3}	2.8×10^{-2}	1.6×10^{-2}	6.5×10^{-3}
Zn	7.5×10^{-1}	6.5×10^{-1}	3.4×10^{-1}	1.9×10^{-1}	2.3×10^{-1}	6.3×10^{-1}	5.7×10^{-1}	4.0×10^{-1}
Pb	1.3×10^{-1}	1.5×10^{-1}	1.1×10^{-1}	4.0×10^{-2}	3.7×10^{-2}	2.0×10^{-1}	1.2×10^{-1}	8.6×10^{-2}
Cu	1.3×10^{-2}	6.3×10^{-2}	7.2×10^{-2}	4.0×10^{-2}	2.4×10^{-2}	6.1×10^{-2}	4.7×10^{-2}	3.7×10^{-2}
As	1.2×10^{-2}	1.3×10^{-2}	2.6×10^{-2}	9.2×10^{-3}	1.3×10^{-2}	2.5×10^{-2}	2.4×10^{-2}	1.1×10^{-2}
Cd	2.8×10^{-3}	3.1×10^{-3}	3.4×10^{-3}	7.4×10^{-4}	1.2×10^{-3}	4.7×10^{-3}	2.7×10^{-3}	1.3×10^{-3}

963

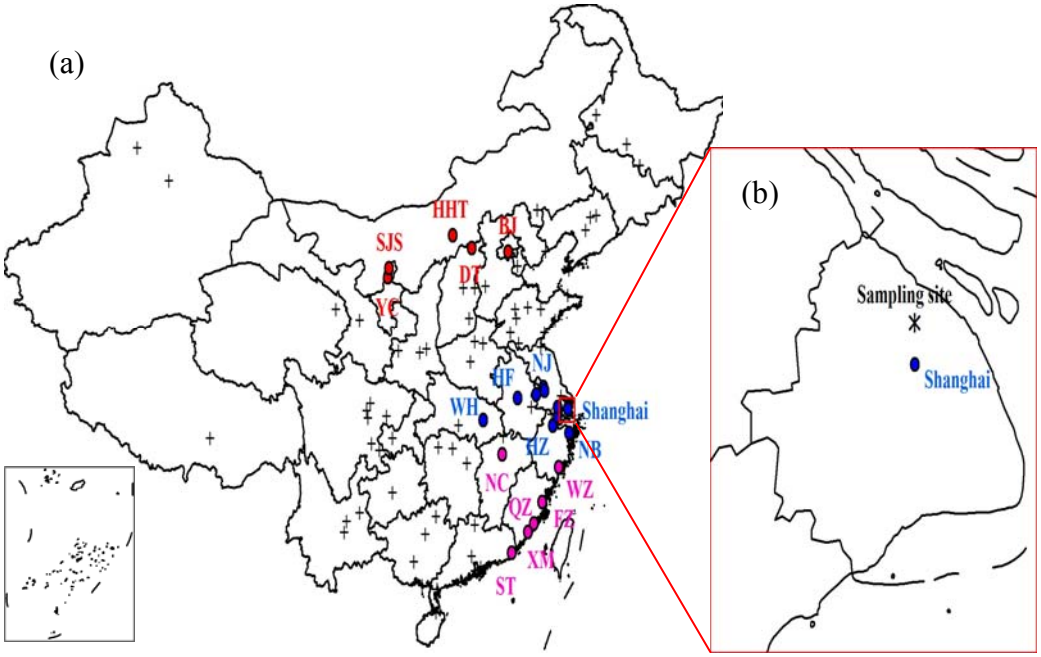

Fig.1 (a) Locations of the 86 major cities over China. The cities with PM_{10} concentrations up to 600μgm^{-3} on March 20, 21, and 22 were marked by red, blue, and pink circles, respectively. (b) The site location of the ground-based measurement in Shanghai.

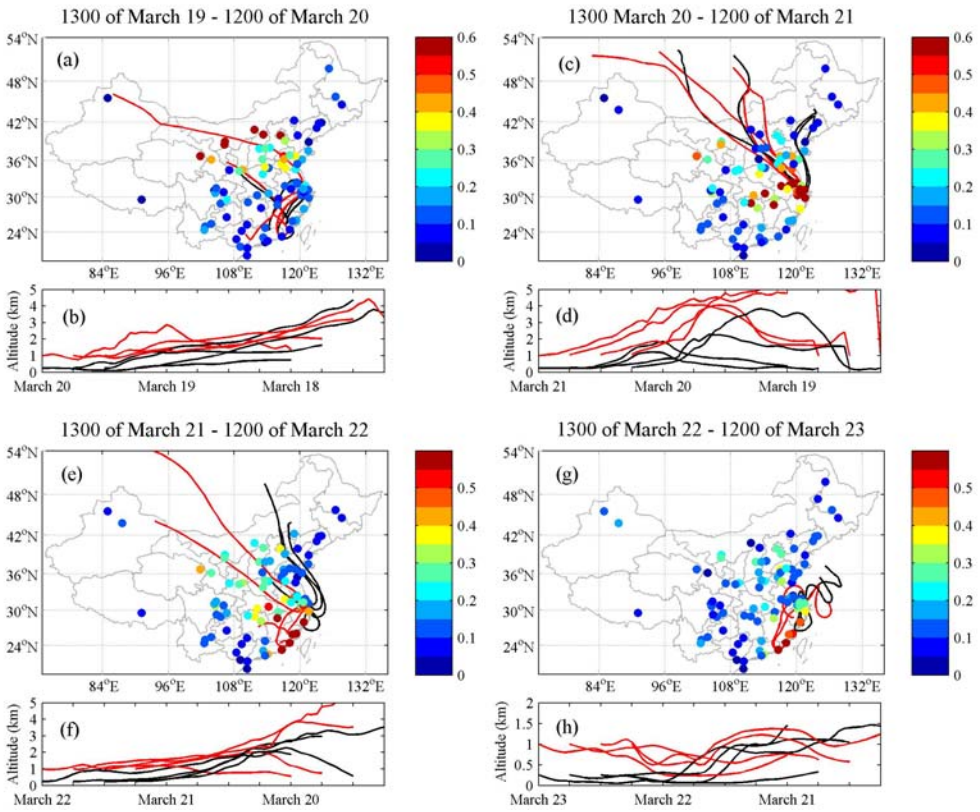

Fig.2 Daily PM_{10} concentrations (mg m^{-3}) in 86 major cities over China and 48 hours backward trajectories of the air masses at both 250m (black lines) and 1000m (red lines) above ground level over Shanghai during March 19-23, 2010. Four trajectories ending at 00, 06, 12, and 18 LST are computed for each day.

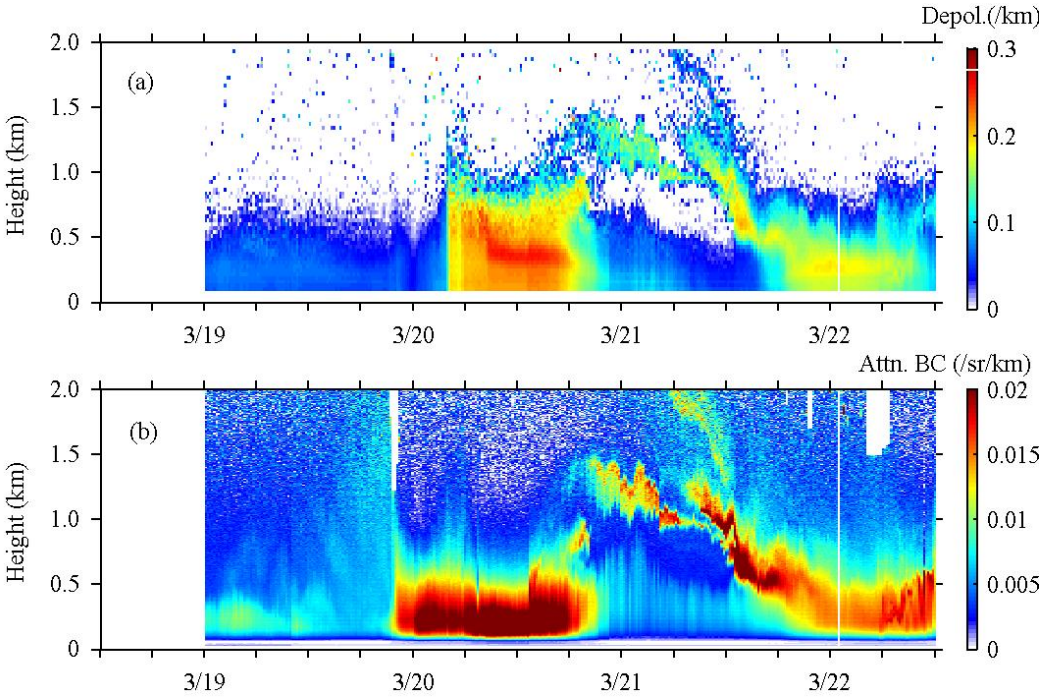

Fig.3 Time-height cross-section of (a) volume depolarization ratios and (b) attenuated aerosol backscattering coefficients measured by a Lidar at the wavelength of 532 nm during March 19-22, 2010 (Local Standard Time).

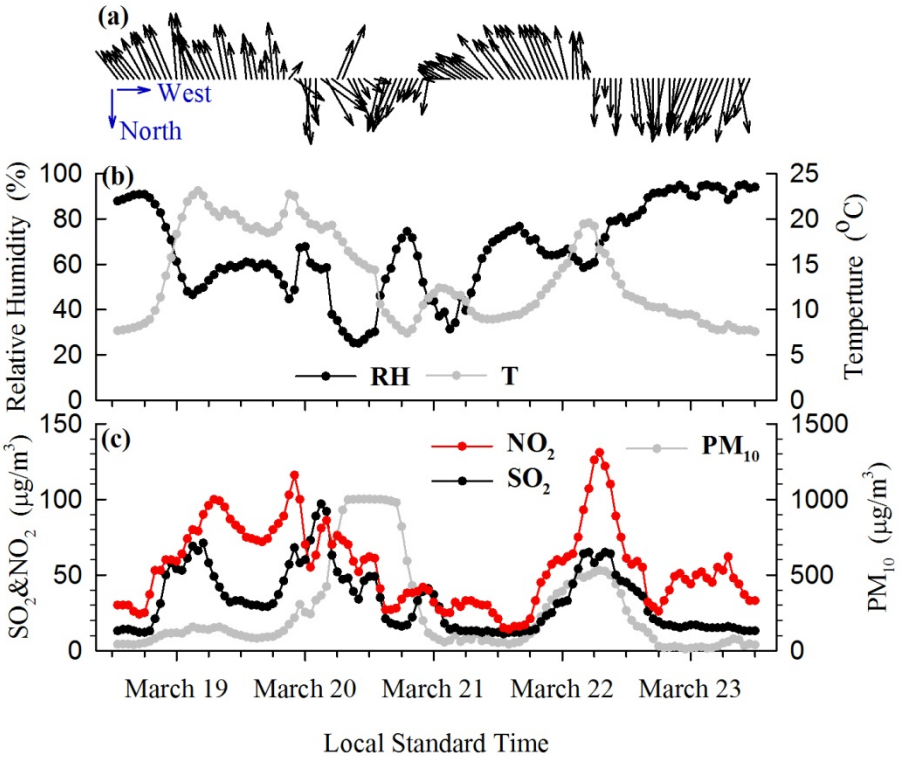

Fig.4 Time-series of PM_{10}, SO_2, NO_2, and meteorological factors including wind conditions, relative humidity (RH), and ambient temperature (T) in Shanghai during March 19-23, 2010.

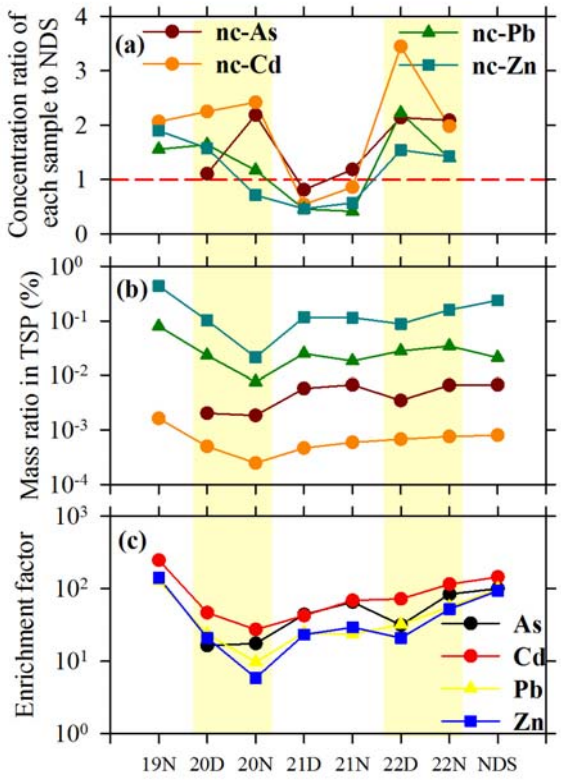

Fig.5 Variations of (a) the mass concentration ratio of each sample to the NDS sample for nc-As, nc-Cd, nc-Pb, and nc-Zn, (b) the mass ratios, and (c) enrichment factors of pollution elements As, Cd, Pb, and Zn in TSP during March 19-22 and non-dust days (NDS). D, N, and NDS represent the daytime samples collected from 8:00 to 20:00 LST, the nighttime samples collected from 20:00 to 8:00 LST in the next day, and the average of the non-dust samples collected from March 25 to 27, respectively.

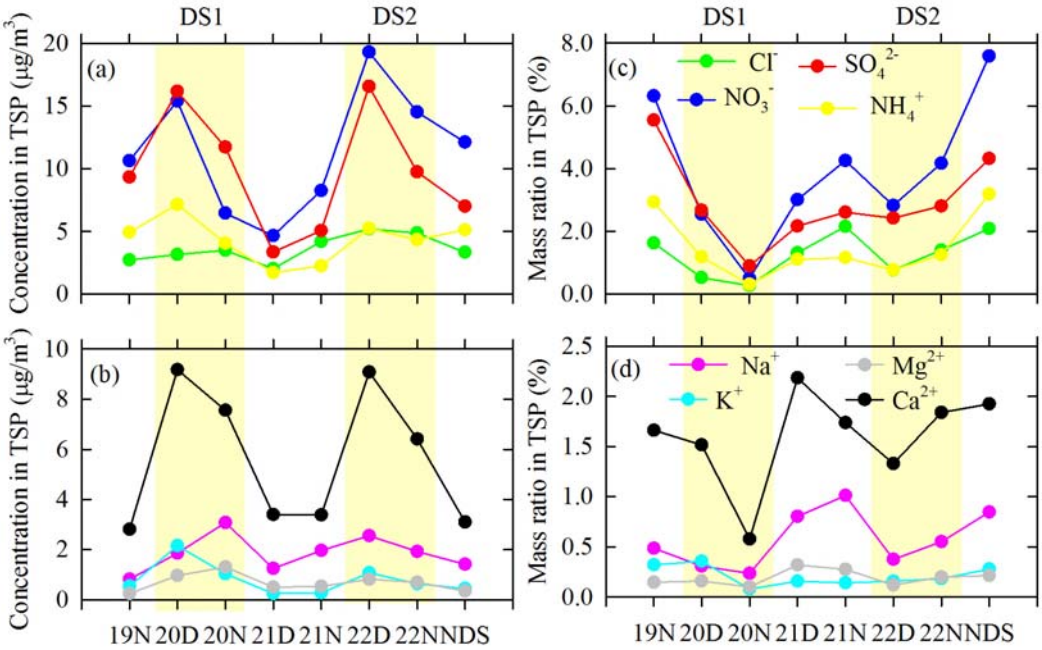

Fig.6 Variations of the concentrations of water-soluble ions and their mass ratios in TSP during March 19-22 and NDS, 2010.

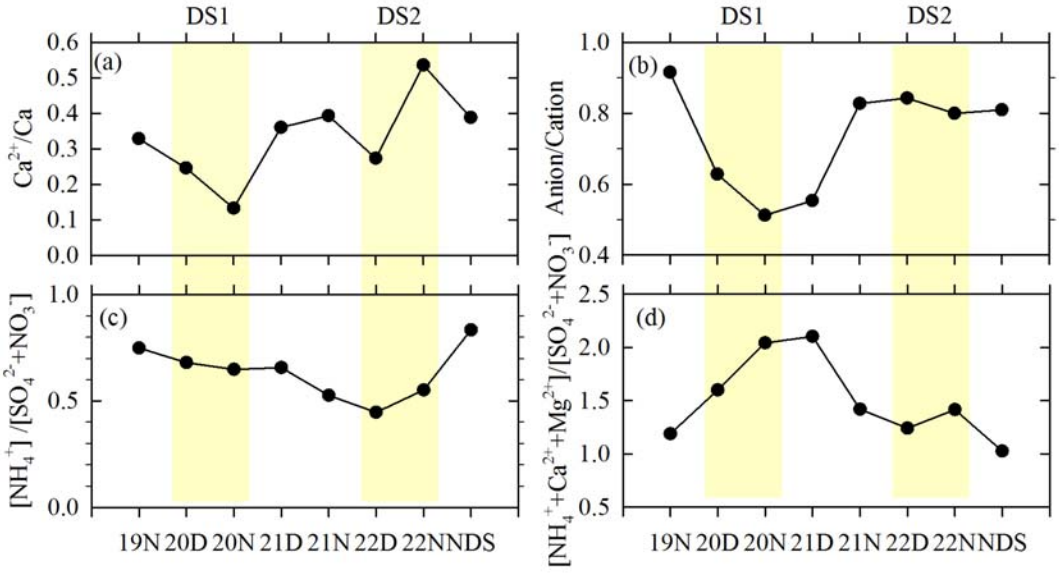

Fig.7 Variations of (a) the ratios of Ca^{2+}/Ca, (b) the equivalent concentrations of the total anions to the total cations (Anion/Cation), (c) the equivalent concentrations of NH_4^+ to the sum of SO_4^{2-} and NO_3^- ($[NH_4^+]/[SO_4^{2-}+NO_3^-]$), and (d) the equivalent concentrations of the sum of NH_4^+, Ca^{2+}, and Mg^{2+} to the sum of SO_4^{2-} and NO_3^- ($[NH_4^+ + Ca^{2+} + Mg^{2+}]/[SO_4^{2-}+NO_3^-]$) in TSP during March 19-22 and NDS, 2010.

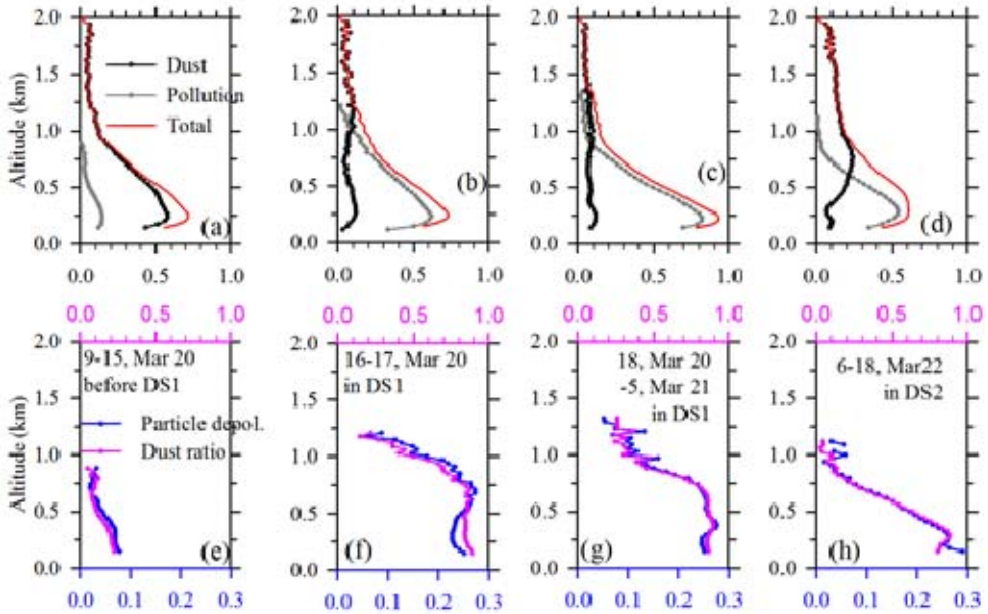

Fig.8 Vertical profiles of the average extinction coefficients of dust, pollution, and total particles (km^{-1}), particle depolarization ratios (Particle depol., unitless), and the ratio of the dust extinction in the total extinction (Dust ratio, unitless) in four periods of 9:00 - 15:00 of March 20 (before DS1), 16:00 - 17:45 of March 20 (before the highest PM_{10} concentration in DS1), 18:00 of March 20 - 4:45 of March 21 (during the highest PM_{10} concentration in DS1), and 6:00 - 18:00 of March 22 in DS2.

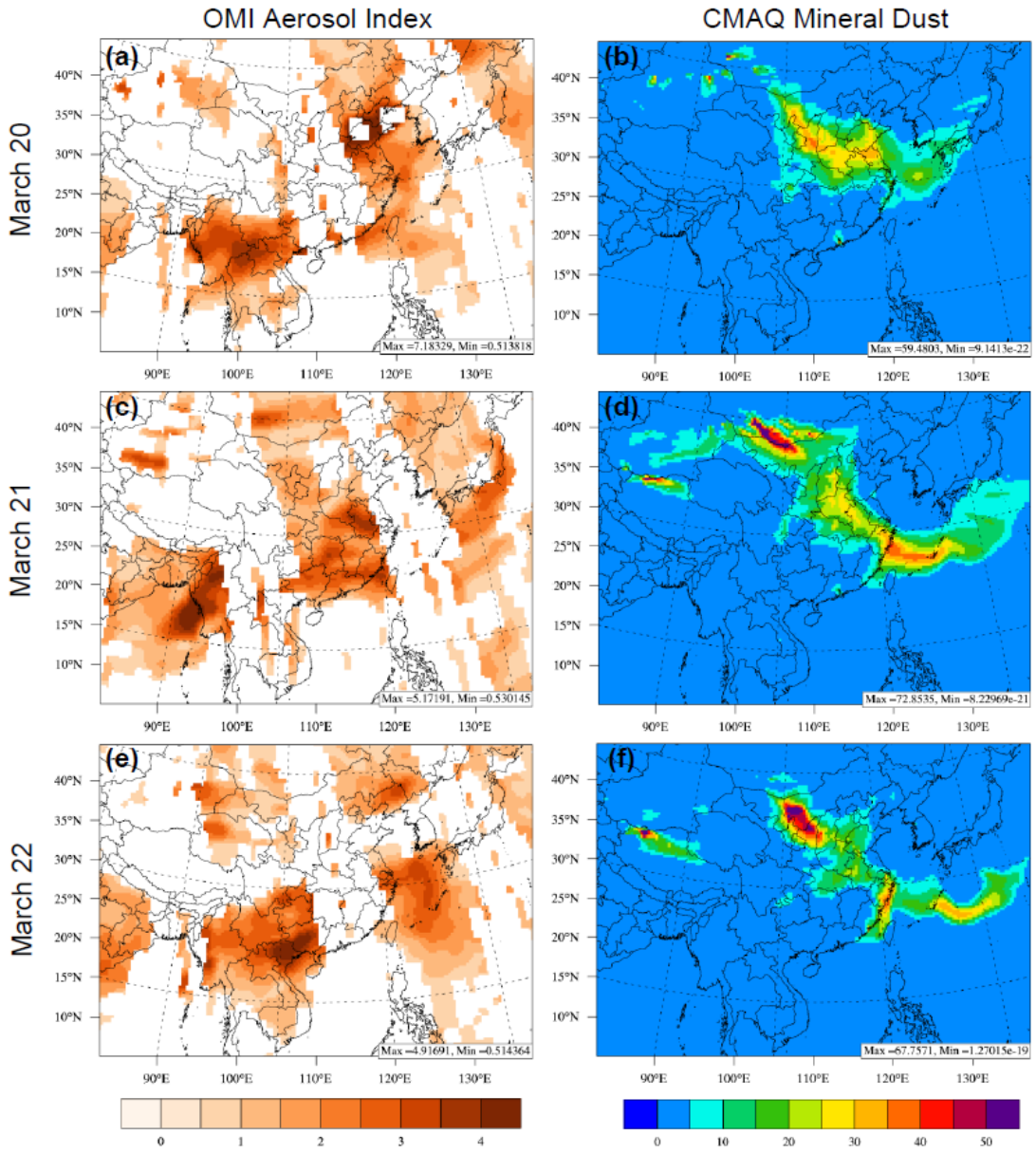

Fig. 9. The spatial distribution of OMI Ultraviolet Aerosol Index (unitless) and simulated mineral aerosols (μgm^{-3}) from March 20 – 22, 2010, respectively.

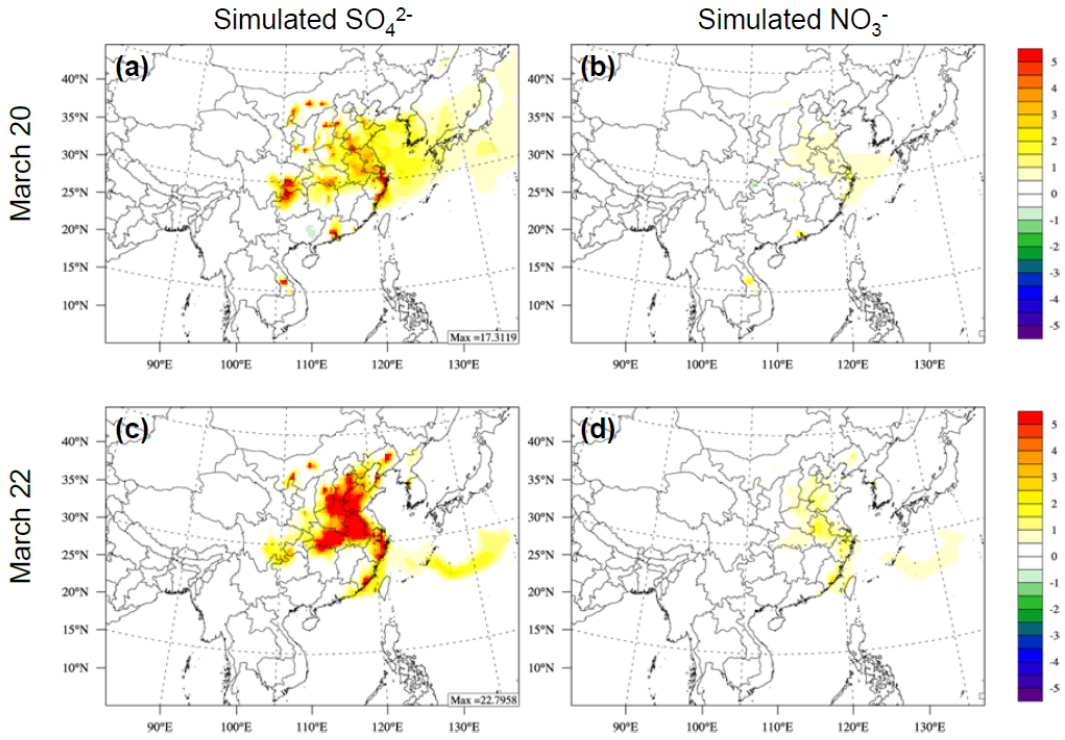

Fig. 10. Simulated SO_4^{2-} and NO_3^- (μgm^{-3}) from dust heterogeneous reactions during DS1 and DS2.